JOURNAL OF PROPULSION AND POWER
Vol. 14, No. 2, March–April 1998

Comparison of Physical and Aerodynamic Ramps as Fuel Injectors in Supersonic Flow

Raymond P. Fuller* and Pei-Kuan Wu†
Taitech, Inc., Wright–Patterson Air Force Base, Ohio 45433
Abdollah S. Nejad‡
U.S. Air Force Research Laboratory, Wright–Patterson Air Force Base, Ohio 45433
and
Joseph A. Schetz§
Virginia Polytechnic Institute and State University, Blacksburg, Virginia 24061

An experimental investigation was conducted to compare the supersonic mixing performance of a novel flush-wall aerodynamic ramp injector with that of a physical ramp injector. The aerodynamic ramp injector consists of nine flush-wall jets arranged to produce fuel–vortex interactions for mixing enhancement in a supersonic crossflow. Test conditions included a Mach 2.0 crossflow of air with a Reynolds number of 3.63×10^7 per meter and helium injection with jet-to-freestream momentum flux ratios of 1.0 and 2.0. Conventional probing techniques, including species composition sampling, were employed to interrogate the flowfield at several downstream locations. Results show that with increasing jet momentum the aeroramp exhibited a significant increase in fuel penetration, whereas the physical ramp showed no discernible change. The near-field mixing of the aeroramp was superior to that of the physical ramp; however, the physical ramp reaches a fully mixed condition at approximately half the distance of the aeroramp. As the jet momentum was increased, the far-field mixing performance of the aeroramp approached that of the physical ramp. In all cases the total pressure loss incurred with the aeroramp was less than that caused by the physical ramp. For both injectors the total pressure loss decreased with increasing jet momentum. It was concluded that, although physical ramps may provide better far-field mixing, properly designed flush-wall injection can provide comparable mixing performance while avoiding the practical problems associated with an intrusive geometry in a scramjet combustor.

Nomenclature

A = cross-sectional area
$\bar{A}$ = relative plume area, $(A - A_u)/(A_s - A_u)$
A_s = stoichiometric plume area, $\boldsymbol{\lambda} A_j/\alpha_s$
A_u = unmixed plume area
C_d = injector discharge coefficient
d_{eff} = effective jet diameter, $C_d^{0.5} d_{\text{eq}}$
d_{eq} = equivalent jet diameter
d_j = jet diameter
h = plume penetration height
M = Mach number
$\dot{m}$ = mass flow rate, $\rho u A$
n = decay rate
P = static pressure
P_{c-s} = cone–static pressure
P_t = total pressure
P_{t2} = pitot pressure
$\bar{q}$ = jet-to-freestream momentum flux ratio, $(\rho u^2)_j/((\rho u^2)_\infty$
T_t = total temperature
U_s = spatial unmixedness
u = flow velocity
X = species mole fraction
x = streamwise axis coordinate
x_{fm} = fully mixed distance
y = spanwise axis coordinate
z = vertical axis coordinate
α = species mass fraction
$\alpha_{\max}$ = maximum helium mass fraction
α_s = stoichiometric mass fraction, 0.0292 for H_2–air
β = decay coefficient
Δ = uncertainty interval
γ = ratio of specific heats
η_m = mixing efficiency
$\boldsymbol{\lambda}$ = jet-to-freestream mass flux ratio, $(\rho u)_j/(\rho u)_\infty$
Π = total pressure loss parameter
ρ = static density

Subscripts
f = fuel property
He = helium property
j = jet exit property
∞ = freestream property

Introduction

SUPERSONIC injection and mixing enhancement are vital to the development of a successful hypersonic air-breathing propulsion system. A successful system will be capable of providing the thrust required to accelerate an aerospace plane or missile from supersonic to hypersonic speeds within Earth's atmosphere. For flight Mach numbers above 5, the adverse effects associated with decelerating the flow to subsonic speeds for combustion prohibit the use of conventional ramjets.[1] Consequently, the use of supersonic combustion ramjets (scramjets) has been proposed. Scramjet combus-

---

Received March 10, 1997; revision received Sept. 20, 1997; accepted for publication Oct. 6, 1997. Copyright © 1997 by the authors. Published by the American Institute of Aeronautics and Astronautics, Inc., with permission.

*Research Scientist, 2372 Lakeview Drive, Suite H. E-mail: fullerrp@possum.appl.wpafb.af.mil. Member AIAA.

†Senior Research Scientist; currently Senior Principal Engineer, Kaiser Marquardt, 16555 Saticoy Street, Van Nuys, CA 91406.

‡Branch Chief, Aero Propulsion and Power Directorate, Experimental Research Branch (POPT); currently Director of Engineering, Kaiser Marquardt, 16555 Saticoy Street, Van Nuys, CA 91406.

§J. Byron Maupin Professor, Department of Aerospace and Ocean Engineering. Fellow AIAA.

tor velocities can be on the order of several thousand meters per second, resulting in severely restricted fuel residence times. A primary concern in hypersonic vehicle development is to limit the engine length and therefore the combustor length caused by weight, skin friction, and heat transfer considerations. This requires an effective fuel injection scheme that will produce enhanced mixing and rapid combustion. A typical scramjet design configuration may include a piloted-flame combustor system with hydrogen as the main fuel. Although hydrogen can provide the heat release necessary to produce sufficient thrust levels, its low molecular weight inhibits fuel penetration and dispersion. Complex injection schemes have, therefore, been developed to effectively disperse the fuel for efficient mixing and combustion, although there usually exists a tradeoff between rapid mixing and total pressure recovery. The objective of the present study is to develop a relatively simple injection scheme capable of providing rapid mixing, stable combustion, and minimized pressure loss.

The subject of transverse and parallel injection of a foreign gas into a supersonic crossflow has been studied extensively in the past.[2-10] A comprehensive review of the mixing of transverse jets and wall jets in supersonic flow has been presented by Schetz et al.[11] Mays et al.[12] studied the effects of low-angle injection into a supersonic flow. It was shown that, as the injection angle decreases, the near-field mixing also decreases. However, this decrease in mixing is accompanied by a desirable reduction of total pressure loss. In the far field, injection angle was found to have little effect on the overall mixing. Fuller et al.[13] extended this work to include injector yaw as well as low transverse angle. It was observed that, although injector yaw did not increase the rate of decay of maximum fuel concentration, it did cause an increase in the overall injectant plume cross section, thus increasing the size of the mixing region. In both studies it was shown that a matched pressure injection condition produced greater fuel concentration decay rates than underexpanded injection.

It has previously been postulated and shown that mixing enhancement may be achieved through the addition of three-dimensional vorticity. Based on experiments performed in the subsonic and transonic regimes, Swithenbank and Chigier[14] proposed that substantial increases in supersonic mixing rates might be obtained by introducing a swirling motion to the fuel. It was postulated that the increase in fuel–air mixing rates would result from the creation of radial and axial pressure gradients in the swirling flow. Povinelli et al.[15] investigated the penetration and spreading of helium injected into the vortex pattern generated by a delta wing in a Mach 2 airstream. Results were compared to a flat-plate injector with the same projected frontal area and angle of attack. It was concluded that the vortex motion generated by the delta wing injector led to substantial increases in the penetration and spreading rates of the injected fuel. In a subsequent study, Hersh and Povinelli[16] obtained similar results for fuel injected into a counter-rotating vortex structure also generated by delta wings. Although these studies demonstrated the effects of swirl on penetration and spreading in a supersonic flow, no experimental data confirming accelerated mixing rates had been produced. In fact, studies later conducted by Povinelli and Ehlers[17] and Schetz and Swanson[18] concluded that, for coaxial jets in supersonic flow, jets with swirl produced no discernible effect on mixing compared with nonswirling jets. However, it is suspected that the swirl number employed in those studies was too small to create radial and axial pressure gradients sufficient for mixing enhancement. The experimental investigation of Tillman et al.[19] concluded that the axial vortex mechanism previously shown to be responsible for rapid mixing in low-speed, subsonic flows can be effective in the supersonic jet environment. Naughton et al.[20] also conducted an experimental study of the effect of streamwise vorticity on supersonic turbulent mixing. A Mach 3, streamwise vortex was generated using a strut-mounted swirl injector exhausting into a Mach 3.5 freestream. Results were compared with a baseline, swirl-free jet. It was found that, with the addition of streamwise vorticity, increases in mixing rates of up to 34% are possible.

Much attention has been given to mechanisms leading to enhanced mixing through the interaction of shock waves with fuel–vortex structures. Marble et al.[21] first proposed the mechanism of shock-induced vorticity generation for supersonic combustion. It was argued that the interaction of a shock wave with a jet of light gas surrounded by an ambient heavy gas would generate vorticity around the perimeter of the jet. This vorticity is caused by the baroclinic torque mechanism that results from a misalignment of the pressure and density gradients at a point in the flow. An excellent review of this process was given by Waitz et al.,[22] and a detailed model was presented by Yang et al.[23] Marble et al.[24] later showed that this phenomenon can lead to a considerable enhancement of the mixing process. They also concluded that some mechanism for destabilizing the vortex must be incorporated into the injector design to ensure complete mixing of the light gas with air. This agrees with the proposal of Naughton et al.[20] that a streamwise vortex can enhance supersonic mixing if the vortical flow is passed through a shock wave of sufficient strength to cause vortex breakdown. Metwally and Settles[25] showed that a strong shock–vortex interaction leading to vortex breakdown is characterized by unsteady upstream shock propagation, apparent flow recirculation, and the appearance of a recompression shock downstream. It was reasoned that such behavior should lead to increased turbulence levels downstream, and therefore enhanced fuel–air mixing.

Numerous investigations[26-31] examined wall ramp injectors as a viable means of providing enhanced fuel–air mixing. Ramp designs attempt to make full use of the various mixing enhancement mechanisms previously discussed (Fig. 1). The ramps provide vortex shedding off the edges and a local separation at the base. The fuel is injected through the base and into the counter-rotating vortex pattern. This situation creates a very dynamic mixing distribution. Furthermore, the ramp shock will reflect from the opposite wall of the combustor and impinge on the fuel–vortex structure, resulting in possible vortex breakdown and further enhancement of the mixing process. The reflected shock also produces baroclinic torque where it intersects the plume, and thus results in additional vorticity production. Finally, the recirculation zone occurring from flow separation at the base of the ramp, like a rearward-facing step, will act as a flame holder. The major drawback to this design is its dependency on maintaining pristine geometry in the ex-

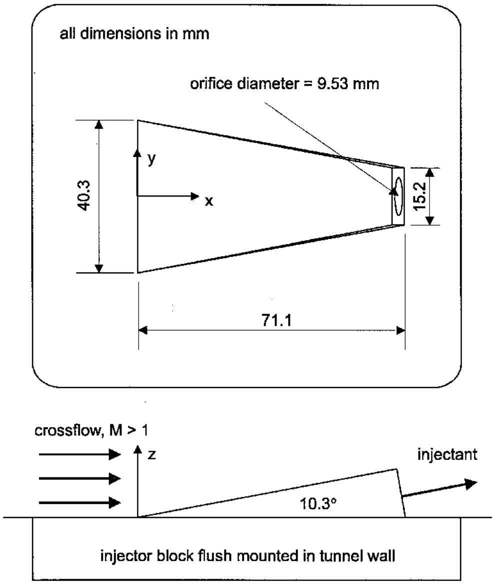

Fig. 1 Physical ramp injector model.

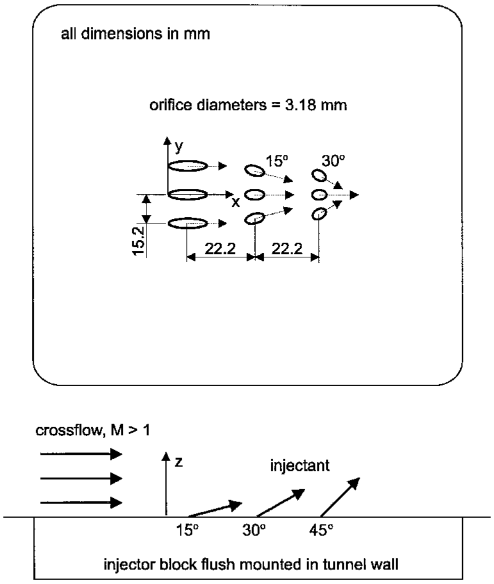

Fig. 2 Aeroramp injector model.

tremely harsh environment of a high-enthalpy scramjet combustor. Its physically intrusive nature will necessarily create hot spots, with temperatures exceeding the thermal limits of most practical materials. Furthermore, the added drag and loss of thrust potential resulting from its intrusive presence may be unacceptable in certain engine design configurations.

The results of the previous studies were the basis for development of the novel injector design concept by Cox et al.[32] given the name aerodynamic ramp, or simply aeroramp. Preliminary results for the aeroramp were first presented by Cox et al. after an investigation involving both experiments and computational fluid dynamics. This injector design consists of a three-by-three array of closely spaced, flush-wall jets with compound injection yaw angles (Fig. 2). The jets were geometrically arranged so as to generate multiplicative fuel–vortex interactions that will lead to enhanced mixing. These fuel–vortex interactions were to include skew-induced vortex generation, shock-induced vortex generation, and vortex breakdown, all of which have been shown to be effective mixing enhancement mechanisms. Furthermore, the flush-wall design coupled with low-angled injection avoids the excessive pressure loss, drag, and hot spots associated with conventional vortex generators.

The objective of the present study was to assess the performance of the aeroramp by comparing it to a physical ramp injector known to provide enhanced mixing in supersonic flow. Tests on both injectors were conducted under the same flow conditions within the same facility. The flowfields generated by each injector were analyzed and described in detail. An array of performance indices were computed to quantify the mixing characteristics of each injector. Finally, two new figures of merit, including a method for the quantification of total pressure loss, were developed.

Experimental Methods

Facilities

The Supersonic Combustion Facility of the Aero Propulsion and Power Directorate at the U.S. Air Force Research Laboratory, Wright–Patterson Air Force Base, was used for all of the experiments described here. Complete details regarding this facility have been presented by Gruber and Nejad.[33] This facility is a continuous-running, open-loop supersonic wind tunnel with a rectangular test section measuring 12.7 cm high, 15.2 cm wide, and 76.2 cm long. A series of compressors capable of providing up to 15 kg/s of air, with total pressures and temperatures up to 4.9 MPa and 920 K, respectively, supply air to the facility. A massive exhaust system lowers and maintains the backpressure for smooth starting and safe operation.

Physical Ramp and Aeroramp Injectors

The physical ramp injector tested in these experiments is based on the design concept first introduced by Northam et al.[26] In the present studies the physical ramp injector (Fig. 1) has a 10.3-deg compression surface with a leading-edge width of 40.3 mm, a trailing-edge width of 15.2 mm, and a length of 71.1 mm. The ramp base is canted at 10.3 deg and contains a 9.53-mm sonic injection orifice, such that the injection axis is parallel to the ramp compression surface.

Figure 2 shows the three-by-three array of sonic jets comprising the aerodynamic ramp injector model. Each circular jet passage has a diameter of 3.18 mm and forms an elliptical orifice at the exit because of the injection angle. The first upstream row of injectors consists of three ports with a spanwise spacing of 9.53 mm, a transverse angle of 15 deg, and no yaw. The second row of injectors is located 22.2 mm downstream of the first row, with a spanwise spacing of 7.94 mm, a transverse angle of 30 deg, and respective yaw angles of −15, 0, and 15 deg. The third row of injectors is located 44.4 mm downstream of the first row, with a spanwise spacing of 6.35 mm, a transverse angle of 45 deg, and respective yaw angles of −30, 0, and 30 deg. The injection insert was designed to be mounted flush with the bottom wall surface of the tunnel test section.

Test Conditions

Tests were conducted with a Mach 2.0 crossflow of air. Freestream conditions were fixed at a total pressure of 310 kPa and a total temperature of 295 K, producing a freestream Reynolds number of 3.63×10^7 per meter. These conditions resulted in a turbulent boundary layer with a thickness of approximately 7 mm at the point of injection. Helium was used as the injectant to simulate hydrogen fuel; $\bar{q}$ was set at either 1.0 or 2.0, as indicated. Recall that $\bar{q}$ is defined by

$$\bar{q} \equiv (\rho u^2)_j/(\rho u^2)_\infty = (\gamma P M^2)_j/(\gamma P M^2)_\infty \tag{1}$$

Neglecting discharge coefficients for the moment, this corresponded to an injection total pressure of 273 kPa for $\bar{q} = 1$, and 545 kPa for $\bar{q} = 2$. For all cases the injectant total temperature was an ambient condition and was, on the average, approximately 295 K.

It was decided that in a real scramjet combustor the physical size of the injector is important; therefore, the origin should be placed at the first point of interaction with the mainstream. If an injector requires a very long length prior to the point of injection, there will be a penalty in the delay of mixing. Therefore, a right-handed, Cartesian coordinate system was chosen, with the origin placed at the leading edge of the injector on the wall surface along the test section centerline (Figs. 1 and 2). The positive x axis was in the freestream direction, the positive z axis was in the vertical direction perpendicular to the wall surface, and the y axis spanned the test section. All lengths were nondimensionalized by d_{eff}, defined as follows:

$$d_{\mathrm{eff}} \equiv C_d^{0.5} d_j \tag{2}$$

For the aeroramp injector, d_{eq} was used in place of d_j. The equivalent diameter was defined as the diameter of a single circular orifice having the same area as the combined area of all nine orifices. This equivalent diameter of the aeroramp was equal to the single jet diameter of the physical ramp; however, the effective diameters were slightly different. The injector discharge coefficients for the physical ramp operating at $\bar{q} = 1$ and 2 were 0.75 and 0.84, respectively. The injector discharge coefficients for the aeroramp operating at $\bar{q} = 1$ and 2 were 0.89 and 0.92, respectively.

For the physical ramp injector, probe measurements were obtained at axial distances of $x = 80$, 118, 213, 518, and 700 mm. For the aeroramp injector, measurements were obtained at axial distances of $x = 65$, 103, 198, 503, and 674 mm. With $\bar{q} = 1$, these distances corresponded to $x/d_{\mathrm{eff}} = 9.7$, 14.3, 25.9, 62.8, and 83.6 for the physical ramp, and $x/d_{\mathrm{eff}} = 7.2$, 11.4, 22.0, 56.0, and 75.0 for the aeroramp. With $\bar{q} = 2$, measurements were obtained at the farthest downstream distance only, corresponding to $x/d_{\mathrm{eff}} = 79.0$ for the physical ramp and $x/d_{\mathrm{eff}} = 73.8$ for the aeroramp.

Instrumentation

Species Composition Sampling

Mean species concentration measurements were obtained using an intrusive sampling probe and gas analyzer designed specifically for use in supersonic flow. The fundamental concepts of this technique have been presented by Ninnemann and Ng.[34] The sampling probe consisted of a small pitot tube with a conical tip and an internal divergence. This geometry was used so that an isokinetic sample could be extracted from the flow. Isokinetic sampling is ensured in supersonic flow by swallowing the shock into the probe. With a swallowed shock, there is no flow disturbance upstream of the probe and no distortion of the stream tube entering the probe inlet. The gas analyzer consisted of a hot-film sensor operating in a channel with a pressure tap and a thermocouple. The sample was drawn into the analyzer using the sampling probe and exhausted out through a choked orifice. The flow through the channel is of very low Mach number, typically 0.05. This allows for the measurement of the total pressure and total temperature within the sampling channel. The gas analyzer is calibrated to measure the helium concentration uniquely related to a given pressure, temperature, and rate of heat transfer sensed at the hot-film operating plane. The absolute measurement uncertainty, relative to the helium mole fraction, was estimated to be ±0.05.

Aerothermodynamic Probing

Mean aerothermodynamic measurements, P_{t2}, P_{c-s}, and T_t, were performed using a standard set of intrusive probes. This set included a pitot probe, a cone–static pressure probe, and a total temperature probe. The pitot probe was a simple round stainless-steel tube with an o.d. of 3.18 mm and an i.d. of 2.37 mm, forming a capture area of 4.29 mm^2. The cone–static pressure probe consisted of a 3.18-mm stainless-steel tube with a closed-end, 10-deg half-angle conical tip. The cone had four pressure taps, each 0.51-mm in diameter, located approximately 7.44 mm from the cone vertex. These pressure taps were spaced azimuthally at 90-deg intervals. All taps emptied into a common chamber to reduce error from flow angularity. The total temperature probe was based on an original design of Winkler.[35] This probe consisted of a 3.18-mm stainless-steel pitot tube with a ceramic diffuser tip. A type-K thermocouple with a 0.38-mm bead was mounted within the ceramic diffuser tip. The diffuser tip had an inlet diameter of 1.60 mm, and two side vent holes with diameters of 0.51 mm each. Geometries were chosen such that the flow entering the probe inlet would be effectively stagnated around the thermocouple bead. This design yielded a temperature recovery factor of approximately 0.98, with a response time constant of approximately 0.01 s.

These three measurements were combined with species composition sampling to determine the average aerothermodynamic variables of interest, e.g., M, P_t, P, T_t, T, ρ, u, etc. Data reduction consisted of an iterative scheme utilizing the isentropic flow relations, perfect gas relations, the Rayleigh–pitot formula, and the Taylor–Mccoll cone flow equation. Details regarding the data reduction have been presented by Fuller et al.[13] The estimated uncertainties (95% confidence interval) in the reduced quantities are as follows: $\Delta P_t = \pm 2.8\%$, $\Delta M = \pm 1.7\%$, $\Delta u = \pm 1.3\%$, $\Delta P = \pm 2.8\%$, $\Delta \rho = \pm 3.0\%$, and $\Delta T = \pm 0.8\%$.

Results and Analysis

Shadowgraphs

Figure 3 shows the shadowgraph images of the physical ramp and aeroramp injectors operating with a $\bar{q}$ of 1.0 or 2.0, as indicated. The main flow is left to right, and the injector is at the bottom of the image. The thin shocks crossing at the extreme left of the images are weak disturbances originating at the interface between the tunnel nozzle and test section. Their angle with respect to the freestream is approximately that of a Mach wave in a Mach 2.0 flow. It is important to bear in mind that these flows are highly three dimensional; careful attention must be given when interpreting the shock structures.

In both Figs. 3a and 3b, the oblique shock wave originating at the leading edge of the physical ramp is clearly seen. The angle of this shock is approximately 38 deg, which is slightly less than the 39.5-deg angle predicted for a 10.3-deg wedge in a Mach 2.0 flow. This is a result of the three-dimensional relieving effect. Just downstream of the top edge of the ramp base, a recompression shock, similar to a lip shock on a rearward-facing step, is observed in both cases. As the flow expands over the ramp base it encounters the jet plume and must negotiate an upward deflection, which results in a recompression wave originating at the fuel–air interface. Farther downstream along the fuel–air interface, the shock wave originating at the upper edge of the jet Mach disk is clearly seen. Note that the barrel shock and Mach disk may not be clearly identified in these photographic reproductions. In the case of $\bar{q} = 1$ (Fig. 3a), two subsequent compression waves following the one formed at the upper edge of the Mach disk can be observed. In the case of $\bar{q} = 2$ (Fig. 3b), however, only the wave originating at the Mach disk is observed, although it is stronger than that observed in the previous case. Various weak shocks appear in the jet plume. These shocks are presumably outside the centerline plane and are a result of three-dimensional effects. (For background on the structure of underexpanded jets in a supersonic crossflow, see Ref. 3.) Finally, note that the observed plume height does not change appreciably when $\bar{q}$ is increased from 1 to 2. This might be expected, because most of the jet momentum is in the freestream direction, although some increase in height should result from a greater expansion of the jet.

In Figs. 3c and 3d, the jet interaction shocks from the aeroramp injector appear as three composite shock structures forming over each of the three rows of jets. In the case of $\bar{q} = 1$ (Fig. 3c), the shocks are curved near the wall and become nearly straight just above the jet plume. The initial angles near the wall, upstream of the first, second, and third rows, are approximately 48, 40, and 38 deg, respectively. All shocks reach a final angle of approximately 35 deg in the field of

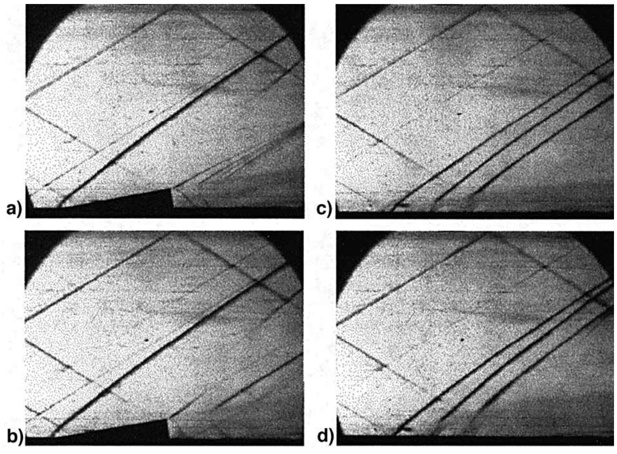

Fig. 3 Shadowgraph images of physical ramp with $\bar{q}$ = a) 1.0 and b) 2.0 and aeroramp with $\bar{q}$ = c) 1.0 and d) 2.0.

view. In the case of $\bar{q} = 2$ (Fig. 3d), the shocks appear to be stronger and the jet penetration has increased significantly compared with the previous case. The shocks are stronger, with initial angles near the wall upstream of the first, second, and third rows of approximately 55, 42, and 41 deg, respectively. Again, all shocks reach a final angle of approximately 35 deg.

Species Composition Sampling

Figure 4 shows the profiles of helium mass fraction at each of the five stations sampled for the physical ramp injector operating with $\bar{q}$ equal to 1.0 or 2.0, as indicated. Note that the contour color scales are not consistent between plots. The minimum value indicating the plume boundary is fixed at a mass fraction value of 0.5%, and the maximum value corresponds to the local station maximum. This rescaling preserves structural details of the plume as the mass fractions vary over 3 orders of magnitude. At $x/d_{\mathrm{eff}} = 9.70$ (Fig. 4a) the jet potential core ($\alpha_{\mathrm{He}} = 1$) persists within the plume. On the left and right sides of the plume there are small triangular structures with low concentrations of helium. These are the effects of the two counter-rotating vortices stripping helium away from the sides of the plume. At $x/d_{\mathrm{eff}} = 14.3$ (Fig. 4b) the plume shape has changed dramatically. The helium has begun to wrap around the vortices and lift away from the wall surface at the centerline. At $x/d_{\mathrm{eff}} = 25.9$ (Fig. 4c) the helium has completely enveloped the vortex structure, with the maximum concentration occurring at the centers of the two vortex cores. At $x/d_{\mathrm{eff}} = 62.8$ (Fig. 4d) the vortex pattern, along with the fuel plume, has convected upward into the freestream. The maximum helium mass fraction is still found at each of the centers of the vortex cores. At $x/d_{\mathrm{eff}} = 83.6$ (Fig. 4e) it is clear that the mixing distribution is no longer dominated by the vortex structure and diffusive mechanisms have taken over. The overall structure of the plume is very similar to that observed in the previous plot, although the overall area of the plume has increased and the maximum helium mass fraction has decreased. Again, the maximum helium concentration is located in what remains of the two vortex cores. In Fig. 4f, $\bar{q}$ was increased to 2 and the last downstream plane of $x/d_{\mathrm{eff}} = 79.0$ was probed. Now, the plume is much fuller, but there is no discernible change in penetration height. Furthermore, there is only a single maximum in the helium concentration, occurring near the plume center, indicating a weaker effect of the dual-vortex structure on the mixing distribution. This should be expected, as the higher jet momentum will tend to lessen the influence of the vortex structure on the fuel plume at a given axial station.

Figure 5 shows the profiles of helium mass fraction at each of the five stations sampled for the aeroramp injector operating with $\bar{q}$ equal to 1.0 or 2.0, as indicated. Again, the contour color scales are varied between plots so as to preserve the structural detail of the plume. At $x/d_{\mathrm{eff}} = 7.21$ (Fig. 5a) three distinct jet cores appear in the single composite plume produced by the entire nine-jet array. These jet cores are produced by the farthest downstream row of jets. The maximum helium concentration is nearly half of the value produced by the physical ramp at $x/d_{\mathrm{eff}} = 9.70$, where the potential core still persists. The diameter of each individual jet comprising the aeroramp is one-third the size of the physical ramp's single orifice. As a result the potential cores of the aeroramp jets will be much shorter than the single potential core of the physical ramp. This will result in a substantially larger decay rate of the helium concentrations in the near field. At $x/d_{\mathrm{eff}} = 11.4$ (Fig. 5b) the three previously distinct jet cores have merged into a single core at the center, with the maximum mass fraction occurring near the wall. At $x/d_{\mathrm{eff}} = 22.0$ (Fig. 5c) the jet core has lifted away from the wall and penetrated farther into the freestream. At $x/d_{\mathrm{eff}} = 56.0$ (Fig. 5d) the jet core has split into two, leaving behind a secondary core in the boundary layer. This was originally identified by Cox et al.[32] as the effect of two large counter-rotating vortices generated by the aeroramp in the very near field. These vortices induce an upward motion at the centerline, disperse helium outward at the top, and entrain air inward near the bottom. This results in the apparent bottlenecking of the plume. At $x/d_{\mathrm{eff}} = 75.0$ (Fig. 5e) the plume has become more rounded, and the two cores that have begun to merge as diffusive mechanisms now dominate the mixing process. In Fig. 5f, $\bar{q}$ was increased to 2 and the last downstream plane of $x/d_{\mathrm{eff}} = 73.8$ was probed. As in the physical ramp case, the higher jet momentum produced a fuller profile; however, unlike the physical ramp case, the penetration increased significantly with jet momentum. At this condition, the penetration is nearly the same as for the physical ramp case. Furthermore, the added jet momentum seems to enhance the vorticity generation as indicated by the increased bottlenecking and separation of the primary and secondary helium cores.

Aerothermodynamic Probing

Figure 6 shows the profiles of total pressure at each of the five stations sampled for the physical ramp injector operating with $\bar{q}$ equal to 1.0 or 2.0, as indicated. In each of the plots shown, the contour color scales are consistent so that plot-to-plot comparisons may easily be made. At $x/d_{\mathrm{eff}} = 9.70$ (Fig.

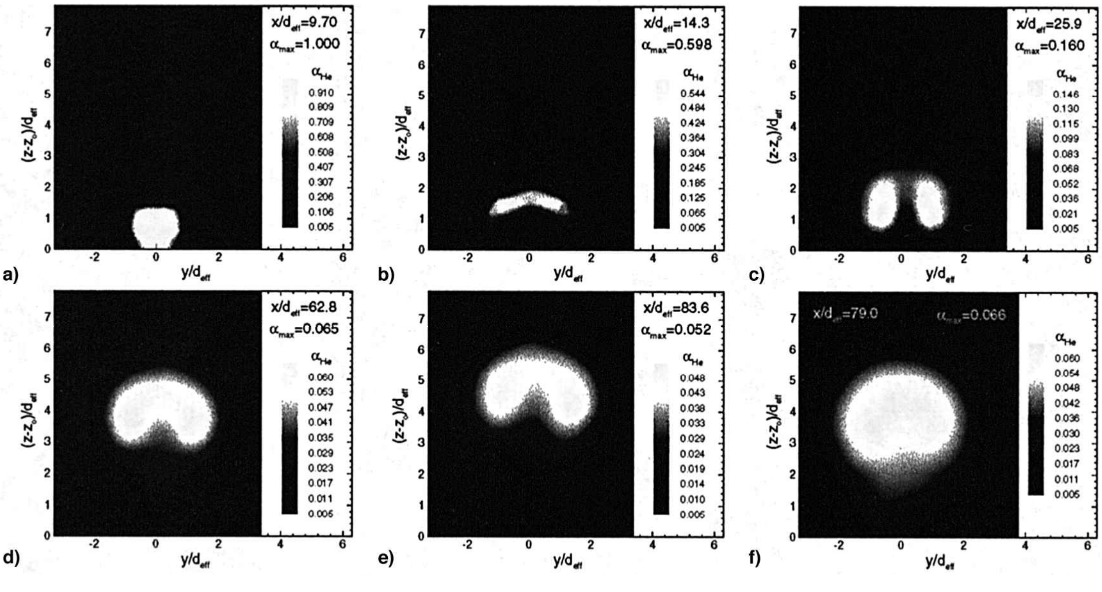

Fig. 4 Helium mass fraction contours for physical ramp injector: a)–e) $\bar{q} = 1$ and f) $\bar{q} = 2$.

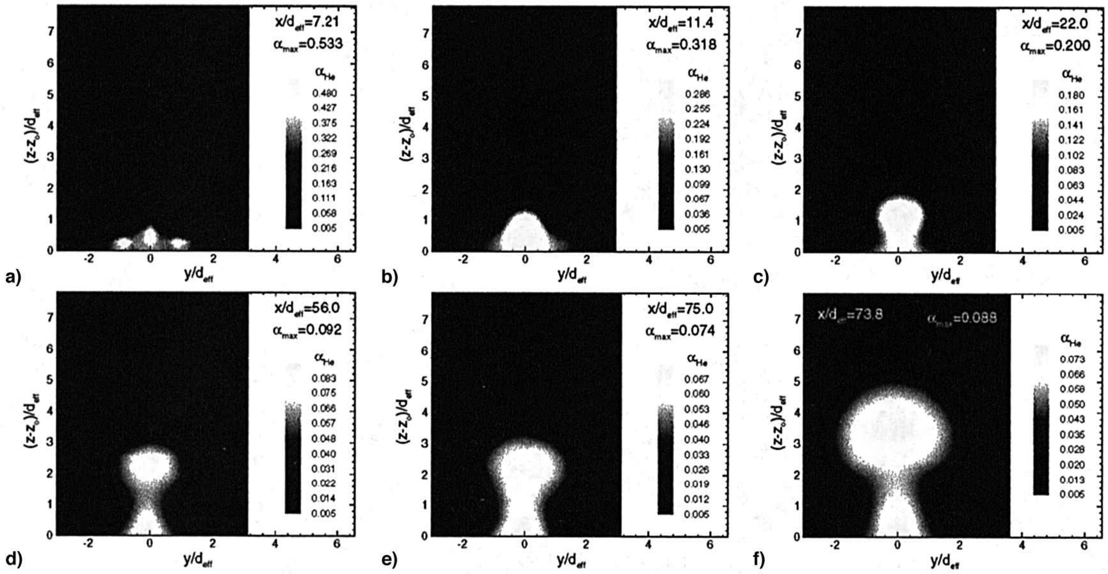

Fig. 5 Helium mass fraction contours for aeroramp injector: a)–e) $\bar{q}$ = 1 and f) $\bar{q}$ = 2.

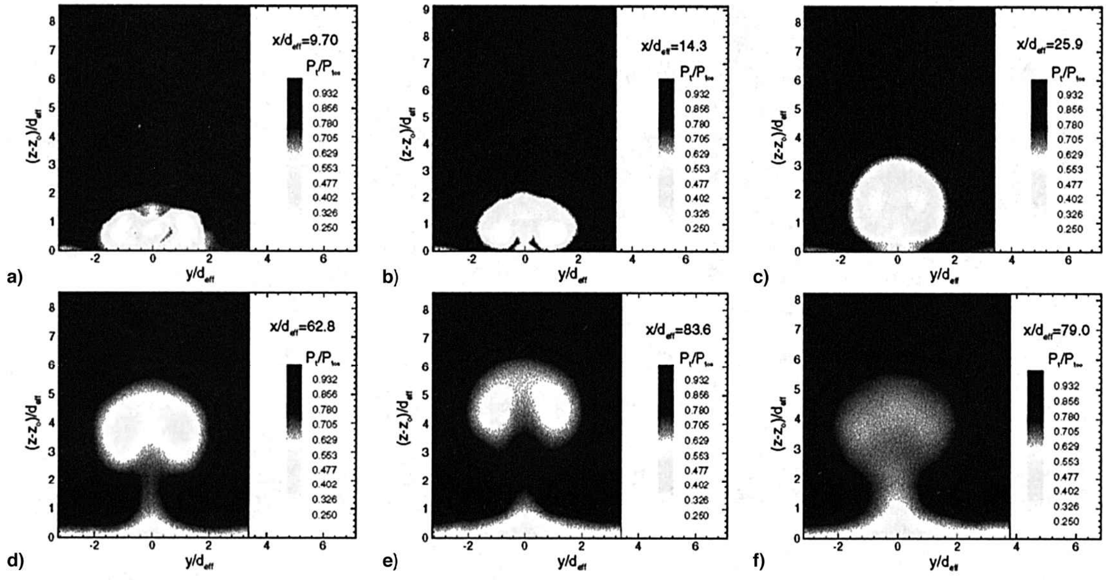

Fig. 6 Total pressure contours for physical ramp injector: a)–e) $\bar{q}$ = 1 and f) $\bar{q}$ = 2.

6a) the effects of the ramp and jet are clearly visible in the plot. Three local minima occur in the plot, corresponding to the two vortex cores and the jet core. The local minimum of total pressure occurring in the jet results from shock losses through the Mach disk. The outer minima clearly identify the locations of the two vortices, where the apparent reduction in total pressure results from a transfer of kinetic energy to the transverse direction. The ramp shock is not apparent in this plot because it was above the vertical extent of measurement. The lip shock, however, can be identified just above the fuel–vortex structure. At x/d_{eff} = 14.3 (Fig. 6b) the losses in the jet core have been distributed over a larger area encompassing the plume, and a certain amount of pressure recovery has been realized. The vortices have retained their strength and position as indicated by the total pressure. The recompression shock downstream of the lip shock can be identified over the fuel–vortex structure. The poor resolution of this shock results from an undesirable interaction with the cone–static pressure probe, leading to slight inaccuracies over the range of impingement. The shock thus appears as a wideband rather than as a discrete step. At x/d_{eff} = 25.9 (Fig. 6c) the vortex structures have convected upward, carrying the plume with them. At x/d_{eff} = 62.8 (Fig. 6d) the losses are less concentrated, indicating a dissipation of the streamwise vorticity. At x/d_{eff} = 83.6 (Fig. 6e) the profile is similar to the previous plot, with smaller gradients and a larger distribution of losses. In Fig. 6f, $\bar{q}$ was increased to 2 and the last downstream plane of x/d_{eff} = 79.0 was probed. As mentioned in the preceding text, the added jet momentum tends to lessen the vorticity generated by the ramp. This is evidenced by the contours, which show only a single core and less severe gradients. Of course, the added jet momentum will also tend to alleviate the losses associated with flow separation and add to the total pressure sensed downstream, which is also evidenced by the contours.

Figure 7 shows the profiles of total pressure at each of the five stations sampled for the aeroramp injector operating with $\bar{q}$ equal to 1.0 or 2.0, as indicated. The contour color scales are consistent between plots. At x/d_{eff} = 7.2 (Fig. 7a) the losses are confined to the boundary layer very near the wall surface. The aeroramp does not appear to separate the boundary layer—at least not to the same extent as was observed with the physical ramp. This will certainly contribute less drag compared with the physical ramp and will minimize the occurrence of hot spots in the vicinity of the injector. The center jet im-

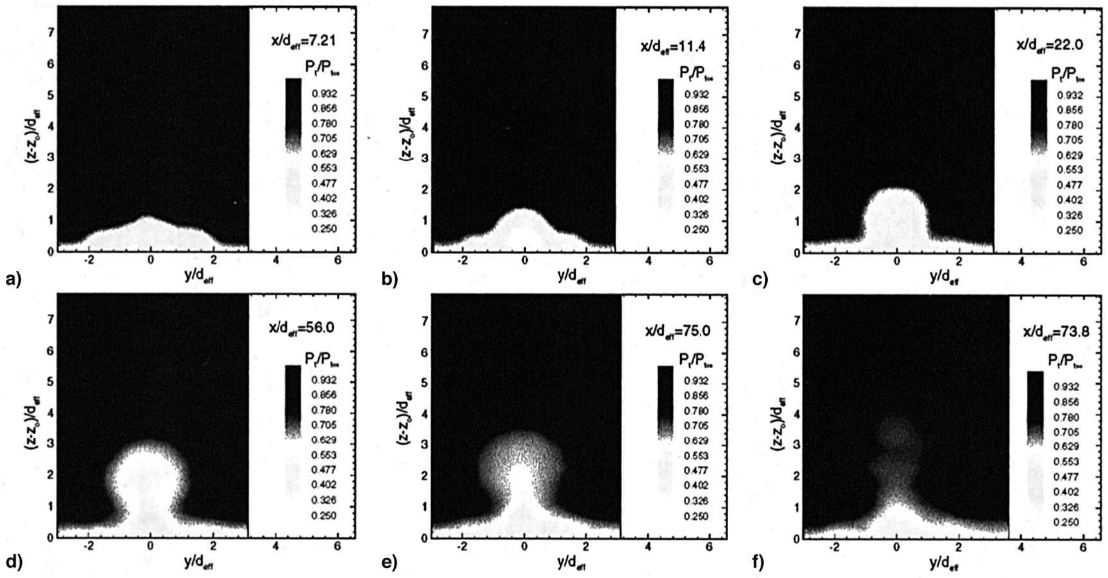

Fig. 7 Total pressure contours for aeroramp injector: a)–e) $\bar{q}$ = 1 and f) $\bar{q}$ = 2.

parts added total pressure to the boundary layer, as indicated by the small local maximum just above the wall at $y/d_{\text{eff}} = 0$ (Fig. 7a). The three composite shock patterns forming over each of the three rows of jets can be identified. As explained in the preceding text, the poor resolution of these shocks results from an undesirable interaction between the jet shock and the cone–static pressure probe shock. The actual shock locations are at the lower edge of these bands, where the jet interaction shock first impinges on the cone–static pressure probe. At $x/d_{\text{eff}} = 11.4$ (Fig. 7b), where the three jets have now merged to form a single core of helium, the total pressure losses are more severe and cover a larger area compared with the previous station. The three composite jet interaction shocks can still be identified and have moved upward with axial distance downstream. At $x/d_{\text{eff}} = 22.0$ (Fig. 7c) some of the total pressure has been recovered within the helium core as the losses have been distributed over a larger region. At $x/d_{\text{eff}} = 56.0$ (Fig. 7d) the jet plume emerges from the boundary layer while a secondary core has developed near the wall. At $x/d_{\text{eff}} = 75.0$ (Fig. 7e) the gradients have become less severe and the pressure losses are distributed over a greater area. Note that no strong vortex patterns appear downstream of the first station. Hence, the mixing downstream of the first station is not dominated by large-scale vorticity, as was the case with the physical ramp. In Fig. 7f, $\bar{q}$ was increased to 2 and the last downstream plane of $x/d_{\text{eff}} = 73.8$ was probed. Note that, although the pressure losses are distributed over a greater area, the magnitude of the losses have been lessened by the added jet momentum. Furthermore, these losses appear to be less severe than those incurred with the physical ramp at $x/d_{\text{eff}} = 79.0$ and $\bar{q} = 2$.

Penetration Trajectory

Overall plume penetration is defined here as the maximum vertical height from the wall surface to the edge of the mixing region, where the fuel mass fraction is 0.5%. The penetration trajectory is then defined as the variation with downstream distance of the plume penetration height. The penetration trajectories of both injectors are quite complicated in the near field, and appear to jump almost discontinuously between $12 < x/d_{\text{eff}} < 22$. To predict penetration accurately in the far-field region, where the trajectories are more well-behaved, curve fits were constructed correlating penetration height with downstream distance for $x/d_{\text{eff}} > 22$ and $\bar{q} = 1$. Past studies have shown the penetration height to vary exponentially with axial distance in the far-field region. Power-law curve fits were constructed using only the data obtained from the last three axial locations. These predictions are shown in Fig. 8 along with the measured penetration heights at each axial location. Also shown are the penetration heights for each injector at the farthest downstream location with $\bar{q} = 2$.

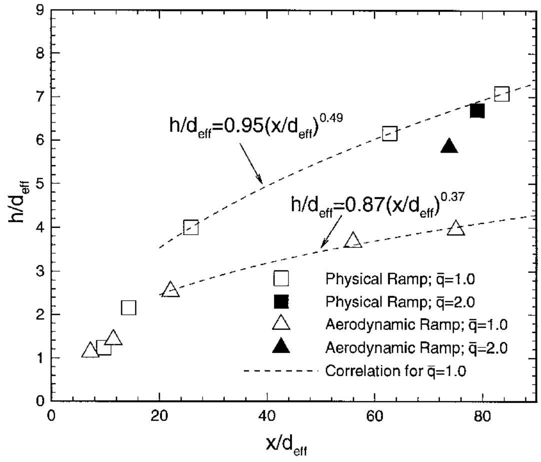

Fig. 8 Injectant penetration trajectory.

Note that when $\bar{q}$ is increased to 2, the normalized penetration for the aeroramp increases, whereas for the physical ramp it decreases. Recall that the penetration is nondimensionalized by d_{eff}, which is a function of the injector discharge coefficient. The increase in $\bar{q}$ results in an increase in the injector discharge coefficient, and therefore in the effective diameter as well. The absolute penetration increases in both cases, although they are scaled by larger effective diameters. These results suggest that, with further increases in $\bar{q}$, the penetration height for the aeroramp may surpass that of the physical ramp. This increase in penetration, however, may also cause the total pressure losses of the aeroramp to approach those of the physical ramp.

Decay of Maximum Concentration

The decay of maximum concentration with downstream distance for the injectors is presented in Fig. 9. In general, the decay of maximum concentration proceeds exponentially with downstream distance, so that it may be correlated using an appropriate power law. The following form will be used to obtain n:

$$\alpha_{\max} = \beta (x/d_{\text{eff}})^{-n} \tag{3}$$

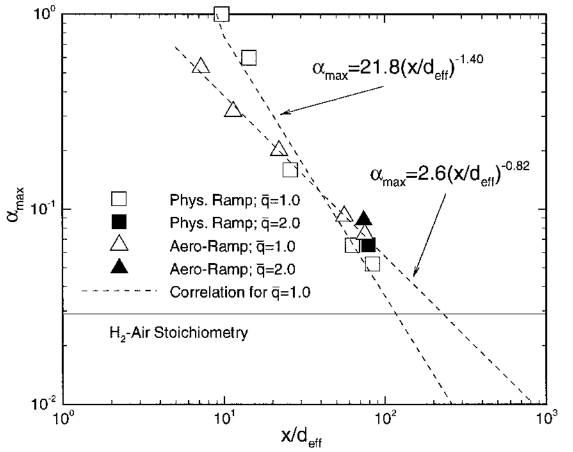

Fig. 9 Decay of maximum concentration vs axial distance.

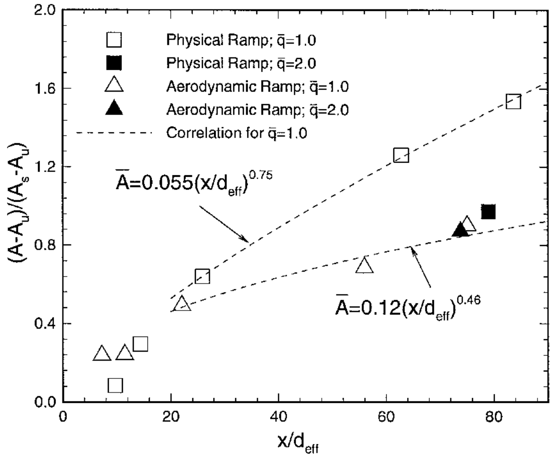

Fig. 10 Relative plume area vs axial distance.

A larger value of n indicates a larger overall rate of decay. Using the data obtained in the experiments, correlations were constructed using the method of least squares. The decay rate for the physical ramp injector was 1.40, and for the aeroramp injector it was 0.82. The physical ramp injector exhibits a very high rate of decay when compared with the average rate of 0.8, determined through an extensive review of jets in crossflow data conducted by Schetz et al.[11] Note, however, that in the near-field region, the initial decay produced by the aeroramp upstream of the first measurement station is superior to that of the physical ramp injector. As a result, the far-field values of maximum concentration are comparable, despite the large decay rate produced by the physical ramp downstream of the first measurement station. Setting $\alpha_{\max} = \alpha_s = 0.0292$, the stoichiometric mass fraction of hydrogen in air, and solving for x/d_{eff}, yields the distance at which all of the mixture is at or below the stoichiometric mass fraction of hydrogen in air. At this distance x_{fm}, the injectant is considered fully mixed. For the physical ramp the fully mixed distance was $113d_{\text{eff}}$, and for the aeroramp it was $240d_{\text{eff}}$.

Plume Area

The overall plume area A is defined here as the area enclosed by the outermost contour representing a fuel mass fraction of 0.5%. Figure 10 shows the relative plume area vs axial distance for each test case. The relative plume area is defined as

$$\bar{A} \equiv (A - A_u)/(A_s - A_u) \tag{4}$$

where A_u is the area to which a segregated jet (a perfectly unmixed jet) would expand if allowed to reach a uniform static pressure equal to the freestream, and A_s is the area required for a uniformly stoichiometric jet to reach the same conditions. The latter is defined by

$$A_s = \boldsymbol{\lambda} A_j/\alpha_s \tag{5}$$

where A_j is the jet exit area. Thus $\bar{A}$ is a measure of the degree to which the plume has expanded. A_u and A_s vary with jet operating conditions. An increase in $P_{t,j}$ results in a linear increase in both A_u and A_s. Therefore, a constant value of $\bar{A}$ with increasing $P_{t,j}$ means that the plume is growing in proportion to $P_{t,j}$.

In the near field, the relative plume area produced by the aeroramp is larger than that produced by the physical ramp. In the far-field region, the plume produced by the physical ramp quickly grows and surpasses the aeroramp plume in terms of size. However, note that when the $\bar{q}$ ratio is increased to 2, $\bar{A}$ decreases significantly for the physical ramp but remains approximately the same size for the aeroramp. That is, the absolute plume area produced by the physical ramp does not grow much with increasing $\bar{q}$, whereas the plume produced by the aeroramp grows significantly. These results suggest that further increases in $\bar{q}$ may lead to a larger plume area for the aeroramp compared with the physical ramp.

Mixing Efficiency

The computation for η_m used here is based on the definition first developed at the NASA Langley Research Center.[36] The mixing efficiency is defined as that fraction of the least available reactant that would react if the fuel–air mixture were brought to chemical equilibrium without additional local or global mixing. Thus, in fuel-rich regions, all of the local air is considered mixed, whereas in fuel-lean regions all of the local fuel is considered mixed. A two-part definition of mixing efficiency is required, depending on whether the flow is globally fuel-rich or fuel-lean. In this particular study of single injectors in a relatively large duct, the flow is globally fuel-lean and η_m is defined as follows:

$$\eta_m \equiv \frac{\dot{m}_{f,\text{mixed}}}{\dot{m}_{f,\text{total}}} = \frac{\displaystyle\int \alpha_r \rho u \, \mathrm{d}A}{\displaystyle\int \alpha \rho u \, \mathrm{d}A} \tag{6}$$

where

$$\alpha_r = \begin{cases} \alpha, & \alpha \leq \alpha_s \\ \alpha_s(1 - \alpha)/(1 - \alpha_s), & \alpha > \alpha_s \end{cases} \tag{7}$$

Note that $\eta_m = 0$ corresponds to a perfectly segregated jet, and $\eta_m = 1$ corresponds to a perfectly mixed system.

Figure 11 shows the integrated mixing efficiencies vs axial distance for both injectors. Fitting a power law to the three downstream points yields predictions for the far-field mixing efficiencies of each injector. In the near field, the mixing efficiency produced by the aeroramp is superior to that produced by the physical ramp. In the far field, however, the mixing efficiency produced by the physical ramp prevails. This is consistent with the results of the maximum fuel concentration and fuel plume area measurements. As $\alpha_{\max}$ decreases and A increases, mixing efficiency must improve. Likewise, if $\alpha_{\max}$ is lower and A is larger in one case compared with another, the mixing efficiency must necessarily be higher. When $\bar{q}$ was increased to 2.0, the mixing efficiencies were reduced in both cases, although the reduction was more severe for the physical ramp. Both injectors rely heavily on streamwise vorticity for mixing enhancement. As stated earlier, the physical ramp vorticity decreases with increasing jet momentum, while for the aeroramp it appears to increase. As a result, further increases

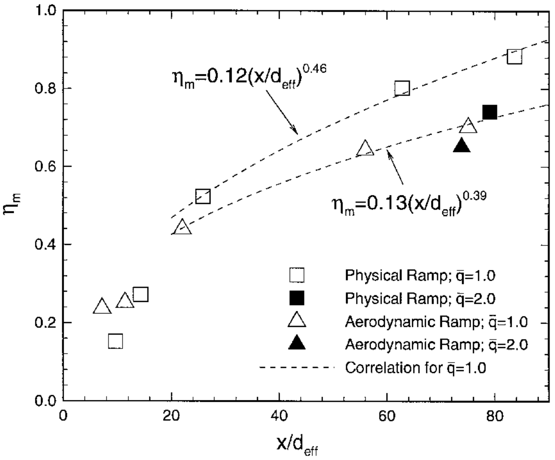

Fig. 11 Mixing efficiency vs axial distance.

in jet momentum will most likely cause the physical ramp to suffer more than the aeroramp in terms of mixing efficiency.

Finally, note that when $\boldsymbol{\alpha}_{\max}$ is less than or equal to α_s, the η_m equals unity. Thus, x_{fm} also corresponds to that distance at which mixing efficiency first reaches unity. The correlations were used to compute the fully mixed distances. For the physical ramp, $x_{\mathrm{fm}} = 100d_{\mathrm{eff}}$, and for the aeroramp, $x_{\mathrm{fm}} = 187d_{\mathrm{eff}}$. These distances are comparable, in terms of relative magnitude, to those computed based on the maximum fuel concentration predictions. The fully mixed distance for the aeroramp is approximately twice the fully mixed distance for the physical ramp. Again, the near-field behavior will most certainly dominate flame ignition characteristics, and the reacting flow will most likely alter the distance required to achieve complete mixing.

Spatial Mixedness

An unmixedness parameter that quantifies mixing rates based on the variance of the concentration distribution was defined by Liscinsky et al.[37] as

$$U_s \equiv \alpha_{\mathrm{var}}/\alpha_{\mathrm{eq}}(1 - \alpha_{\mathrm{eq}}) \tag{8}$$

$$\alpha_{\mathrm{var}} = \frac{1}{n}\sum_{i=1}^{n}(\bar{\alpha}_i - \alpha_{\mathrm{eq}})^2 \tag{9}$$

$$\alpha_{\mathrm{eq}} = \dot{m}_j/(\dot{m}_j + \dot{m}_\infty) \tag{10}$$

$$\bar{\alpha}_i = \alpha_i\alpha_{\mathrm{eq}}\left(\frac{1}{n}\sum_{i=1}^{n}\alpha_i\right)^{-1} \tag{11}$$

A value of zero for U_s corresponds to a perfectly mixed system, and a value of unity corresponds to a perfectly segregated system. The value of this parameter is that it is based on fuel concentration measurements only and does not rely on aerothermodynamic measurements. It was originally developed for planar-laser fuel plume imaging. Here, we have chosen to plot $1 - U_s$, so as to be consistent with the information provided by the plume area and mixing efficiency (i.e., a larger value indicates better mixing).

Figure 12 shows the computed spatial mixedness $1 - U_s$ vs axial distance, along with the correlations for both injectors tested. The fully mixed distances, where $U_s = 0$, based on the correlations are $x_{\mathrm{fm}} = 120d_{\mathrm{eff}}$ for the physical ramp and $x_{\mathrm{fm}} = 218d_{\mathrm{eff}}$ for the aeroramp. Again, the distances are comparable to those previously computed using the maximum concentration and mixing efficiency correlations. When $\bar{q}$ was increased to 2 the spatial mixedness decreased with the physical ramp, while it increased slightly for the aeroramp, yet again indicating better mixing performance with increasing $\bar{q}$ for the aeroramp.

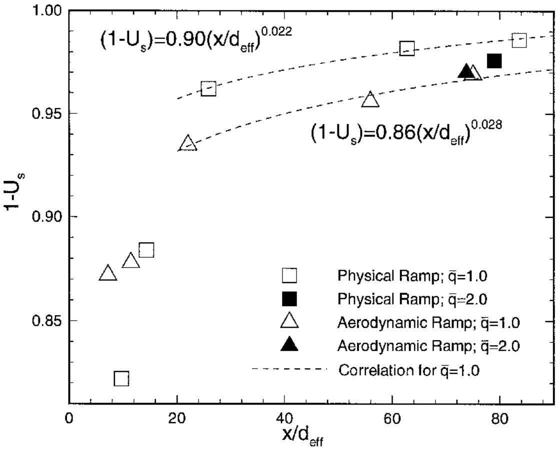

Fig. 12 Spatial mixedness vs axial distance.

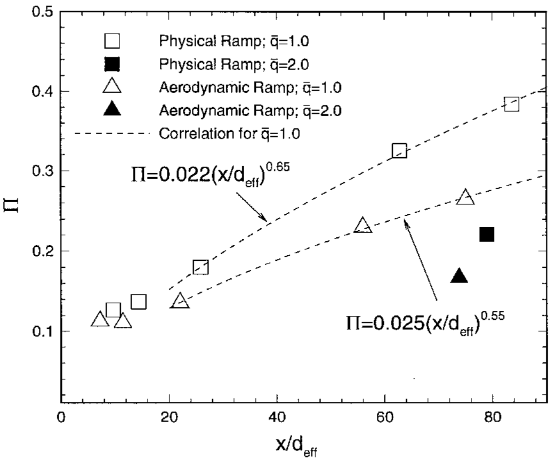

Fig. 13 Total pressure loss parameter vs axial distance.

Total Pressure Losses

The total pressure losses caused by fuel injection can seriously affect the thermodynamic efficiency of a scramjet engine. Therefore, the evaluation of a given injector must include some quantification of losses. The total pressure of the incoming air is reduced by viscous forces in the boundary layer, shock waves, flow separation, and fuel–air mixing. Unfortunately, these losses are often very difficult to assess in the cold-flow situation. Previous studies conducted by Fuller et al.[13] and Mays et al.[38] defined quantitative measures for such assessments. In each case losses were quantified by examining the mass-weighted field values of the total pressure normalized by the freestream conditions. However, the area over which the integration takes place was either facility-dependent or based on a complex analysis of data not readily available. To simplify these measures, an adaptation of those previously defined forms was developed. Π was defined here as

$$\Pi = \frac{\int \rho u(P_{t,\infty} - P_t)\,\mathrm{d}A}{\rho_\infty u_\infty P_{t,\infty}A_s + \rho_j u_j P_{t,j}A_j} \tag{12}$$

where A_s is the previously defined stoichiometric area of Eq. (5). A parameter value of $\Pi = 0$ indicates no losses. However, the total pressure parameter is essentially unbounded and a value of unity does not indicate total loss.

The computed total pressure loss parameter vs axial distance for each injector has been plotted in Fig. 13. Again, power-law curve fits have been constructed using the last three data points. The pressure loss incurred with the physical ramp injector is more severe than that exhibited by the aeroramp injector for both cases of $\bar{q}$ equal to 1 and 2. Note that when $\bar{q}$ is increased from 1 to 2, there is an apparent reduction in total pressure loss, as also indicated in the total pressure contours. These reductions are a result of the increased contributions made by the jet to the axial momentum. The reduction in the case of the physical ramp is greater; this should be expected because a much greater part of the jet momentum, compared with the aeroramp, is in the axial direction.

Summary and Conclusions

An experimental investigation was conducted to compare the performance of the aeroramp injector with a physical ramp injector previously shown to enhance mixing in supersonic flow. The scope of the investigation focused on jet penetration, mixing characteristics, and total pressure losses. Several analysis techniques were applied to evaluate the mixing characteristics and all provided consistent results. Furthermore, a parameter was defined to quantify the total pressure losses without complex analysis or facility dependence.

The mixing characteristics of the physical ramp injection were dominated by the counter-rotating vortices generated by the ramp. The fuel–air mixing produced by the aeroramp was dominated by the multiplicative fuel–vortex interactions confined to the immediate injector vicinity. Mixing effectiveness was evaluated based on fuel penetration, maximum fuel mass fraction decay, plume area, mixing efficiency, and spatial mixedness. With a $\bar{q}$ of unity the aeroramp produced superior mixing in the near field and inferior mixing in the far field. With a $\bar{q}$ of 2 the aeroramp mixing approached that of the physical ramp in the far field. The enhanced mixing of the aeroramp can be attributed to the multiplicative fuel–vortex interactions in the near field as well as the multiple jet design. That is, several small jets should mix better than one single jet. The enhanced mixing of the physical ramp can be attributed to the counter-rotating vortex pair. Increasing the jet momentum reduced the effect of the vortices produced by the physical ramp, whereas it increased the strength of the interactions produced by the aeroramp. Thus, with increasing jet momentum, the overall mixing performance decreased for the physical ramp, while it increased for the aeroramp.

Total pressure loss was quantified by applying the newly defined pressure-loss parameter. For the physical ramp the total pressure losses were concentrated around the centers of the two counter-rotating vortices. For the aeroramp the total pressure losses were concentrated around the core of the jet plume. The overall pressure loss suffered by the physical ramp was more severe than the pressure loss of the aeroramp. With a $\bar{q}$ of unity, the physical ramp exhibited a larger loss parameter over the entire axial range of measurements. When $\bar{q}$ was increased to 2, both injectors exhibited a reduction in losses.

Acknowledgments

This work was sponsored by and performed at the U.S. Air Force Research Laboratory, Wright–Patterson Air Force Base, Ohio, under Contracts F33615-93-C-2300 and F33615-96-C-2625. The experimental work was made possible through the efforts of T. Chen, G. Haines, M. Landrum, and D. Schommer of Taitech, Inc., and M. Gruber of the U.S. Air Force Research Laboratory. Editorial consulting was provided by A. Creese of Taitech, Inc. Technical monitoring was provided by J. Donbar and D. Glawe of the U.S. Air Force Research Laboratory. Finally, sincere appreciation is given to the Air Facilities Group at the U.S. Air Force Research Laboratory Aero Propulsion and Power Directorate.

References

[1] Heiser, W. H., Pratt, D. T., Daley, D. H., and Mehta, U. B., *Hypersonic Airbreathing Propulsion*, edited by J. S. Przemieniecki, *AIAA Education Series*, AIAA, Washington, DC, 1994.

[2] Schetz, J. A., and Billig, F. S., "Penetration of Gaseous Jets Injected into a Supersonic Stream," *Journal of Spacecraft and Rockets*, Vol. 3, No. 11, 1966, pp. 1658–1665.

[3] Schetz, J. A., Hawkins, P. F., and Lehman, H., "Structure of Highly Underexpanded Transverse Jets in a Supersonic Stream," *AIAA Journal*, Vol. 5, No. 5, 1967, pp. 882–884.

[4] Schetz, J. A., Weinraub, R. A., and Mahaffey, R. E., Jr., "Supersonic Transverse Injection into a Supersonic Stream," *AIAA Journal*, Vol. 6, No. 5, 1968, pp. 933, 934.

[5] Schetz, J. A., "Interaction Shock Shape for Transverse Injection," *Journal of Spacecraft and Rockets*, Vol. 7, No. 2, 1970, pp. 143–149.

[6] Gruber, M. R., Nejad, A. S., Chen, T. H., and Dutton, J. C., "Mixing and Penetration Studies of Sonic Jets in a Mach 2 Freestream," *Journal of Propulsion and Power*, Vol. 11, No. 2, 1995, pp. 315–323.

[7] Barber, M. J., Roe, L. A., and Schetz, J. A., "Simulated Fuel Injection Through a Wedge-Shaped Orifice into Supersonic Flow," AIAA Paper 95-2559, July 1995.

[8] Glawe, D. D., Samimy, M., Nejad, A. S., and Chen, T. H., "Effects of Nozzle Geometry on Parallel Injection into a Supersonic Flow," *Journal of Propulsion and Power*, Vol. 12, No. 6, 1996, pp. 1159–1168.

[9] Gruber, M. R., Nejad, A. S., Chen, T. H., and Dutton, J. C., "Large Structure Convection Velocity Measurements in Compressible Transverse Injection Flowfields," *Experiments in Fluids* (to be published).

[10] Gruber, M. R., Nejad, A. S., Chen, T. H., and Dutton, J. C., "Compressibility Effects in Supersonic Transverse Injection Flowfields," *Physics of Fluids*, Vol. 9, No. 5, 1966, pp. 1448–1461.

[11] Schetz, J. A., Thomas, R. H., and Billig, F. S., "Mixing of Transverse Jets and Wall Jets in Supersonic Flow," *Separated Flows and Jets*, edited by V. V. Kozlov and A. V. Dovgal, Springer–Verlag, Berlin, 1991.

[12] Mays, R. B., Thomas, R. H., and Schetz, J. A., "Low Angle Injection into a Supersonic Flow," AIAA Paper 89-2461, July 1989.

[13] Fuller, E. J., Thomas, R. H., and Schetz, J. A., "Mixing Studies of Helium in Air at High Supersonic Speeds," *AIAA Journal*, Vol. 30, No. 9, 1992, pp. 2234–2243.

[14] Swithenbank, J., and Chigier, N. A., "Vortex Mixing for Supersonic Combustion," *12th Symposium (International) on Combustion* (Poitiers, France), The Combustion Inst., Pittsburgh, PA, 1969, pp. 1153–1162.

[15] Povinelli, L. A., Povinelli, F. P., and Hersch, M., "A Study of Helium Penetration and Spreading in a Mach 2 Airstream Using a Delta Wing Injector," NASA TN D-5322, July 1969.

[16] Hersch, M., and Povinelli, L. A., "Effect of Interacting Vortices on Jet Penetration into a Supersonic Stream," NASA TM-X-2134, Nov. 1970.

[17] Povinelli, L. A., and Ehlers, R. C., "Swirling Base Injection for Supersonic Combustion Ramjets," *AIAA Journal*, Vol. 10, No. 9, 1972, pp. 1243, 1244.

[18] Schetz, J. A., and Swanson, R. C., "Turbulent Jet Mixing at High Supersonic Speeds," *Zeitschrift für Flugwissenschaften*, Vol. 21, No. 5, 1973, pp. 166–173.

[19] Tillman, T. G., Patrick, W. P., and Paterson, R. W., "Enhanced Mixing of Supersonic Jets," *Journal of Propulsion and Power*, Vol. 7, No. 6, 1991, pp. 1006–1014.

[20] Naughton, J. W., Cattafesta, L. N., and Settles, G. S., "An Experimental Study of the Effect of Streamwise Vorticity on Supersonic Mixing Enhancement," AIAA Paper 92-3549, July 1992.

[21] Marble, F. E., Hendricks, G. J., and Zukoski, E. E., "Progress Toward Shock Enhancement of Supersonic Combustion Processes," AIAA Paper 87-1880, June 1987.

[22] Waitz, I. A., Marble, F. E., and Zukoski, E. E., "Vorticity Generation by Contoured Wall Injectors," AIAA Paper 92-3550, July 1992.

[23] Yang, J., Kubota, T., and Zukoski, E. E., "A Model for Characterization of a Vortex Pair Formed by Shock Passage over a Light-Gas Inhomogeneity," *Journal of Fluid Mechanics*, Vol. 258, 1994, pp. 217–244.

[24] Marble, F. E., Zukoski, E. E., Jacobs, J. W., Hendricks, G. J., and Waitz, I. A., "Shock Enhancement and Control of Hypersonic Mixing and Combustion," AIAA Paper 90-1981, July 1990.

[25] Metwally, O., and Settles, G., "An Experimental Study of Shock Wave/Vortex Interaction," AIAA Paper 89-0082, Jan. 1989.

[26] Northam, G. B., Greenburg, I., Byington, C. S., and Capriotti, D.

P., "Evaluation of Parallel Injector Configurations for Mach 2 Combustion," *Journal of Propulsion and Power*, Vol. 8, No. 2, 1992, pp. 491–499.

[27] Davis, D. O., and Hingst, W. R., "Progress Toward Synergistic Hypermixing Nozzles," AIAA Paper 91-2264, June 1991.

[28] Waitz, I. A., Marble, F. E., and Zukoski, E. E., "Investigation of a Contoured Wall Injector for Hypervelocity Mixing Augmentation," *AIAA Journal*, Vol. 31, No. 6, 1993, pp. 1014–1021.

[29] Hartfield, R. J., Hollo, S. D., and McDaniel, J. C., "Experimental Investigation of a Supersonic Swept Ramp Injector Using Laser-Induced Iodine Fluorescence," *Journal of Propulsion and Power*, Vol. 10, No. 1, 1994, pp. 129–135.

[30] Riggins, D. W., McClinton, C. R., Rogers, R. C., and Bittner, R. D., "Investigation of Scramjet Strategies for High Mach Number Flows," *Journal of Propulsion and Power*, Vol. 11, No. 3, 1995, pp. 409–418.

[31] Riggins, D. W., and Vitt, P. H., "Vortex Generation and Mixing in Three-Dimensional Supersonic Combustors," *Journal of Propulsion and Power*, Vol. 11, No. 3, 1995, pp. 419–425.

[32] Cox, S. K., Fuller, R. P., Schetz, J. A., and Walters, R. W., "Vortical Interactions Generated by an Injector Array to Enhance Mixing in Supersonic Flow," AIAA Paper 94-0708, Jan. 1994.

[33] Gruber, M. R., and Nejad, A. S., "New Supersonic Combustion Research Facility," *Journal of Propulsion and Power*, Vol. 11, No. 5, 1994, pp. 1080–1082.

[34] Ninnemann, T. A., and Ng, W. F., "A Concentration Probe for the Study of Mixing in Supersonic Shear Flows," *Experiments in Fluids*, Vol. 13, No. 2-3, 1992, pp. 98–104.

[35] Winkler, E. M., "Design and Calibration of Stagnation Temperature Probes for Use at High Supersonic Speeds and Elevated Temperatures," *Journal of Applied Physics*, Vol. 25, No. 2, 1954, pp. 231–232.

[36] Mao, M., Riggins, D. W., and McClinton, C. R., "Numerical Simulation of Transverse Fuel Injection," NASP CR-1089, May 1990.

[37] Liscinsky, D. S., True, B., and Holdeman, J. D., "Effects of Initial Conditions on a Single Jet in Crossflow," AIAA Paper 95-2998, July 1995.

[38] Mays, R. B., Thomas, R. H., and Schetz, J. A., "Experimental Investigation of Sonic Helium Injection at a Low Downstream Angle into a Supersonic Flow," Virginia Polytechnic Inst. and State Univ., Paper VPI-AOE-171, Blacksburg, VA, June 1990.

Color reproductions courtesy of Taitech, Inc.